Quantitative Analysis of Coupled Carbon and Energy Metabolism for Lignin Carbon Utilization in *Pseudomonas putida*

Nanqing Zhou,[1] Rebecca A. Wilkes,[2] Xinyu Chen,[1] Kelly P. Teitel,[1] James A. Belgrave,[3] Gregg T. Beckham,[2] Allison Z. Werner,[2] Yanbao Yu,[4] Ludmilla Aristilde[1,3,*]

[1]Department of Civil and Environmental Engineering, McCormick School of Engineering and Applied Science, Northwestern University, Evanston, IL 60208, USA; [2]Renewable Resources and Enabling Sciences Center, National Renewable Energy Laboratory, Golden, CO, USA; [3]Northwestern Center for Synthetic Biology, Northwestern University, Evanston, IL 60208, USA; [4]Department of Chemistry and Biochemistry, University of Delaware, Newark, DE 19716, USA

*Corresponding author: ludmilla.aristilde@northwestern.edu

Keywords: lignin-derived aromatics | multi-omics | carbon metabolism | cofactors | *Pseudomonas putida*

Soil *Pseudomonas* species, which can thrive on lignin-derived phenolic compounds, are widely explored for biotechnology applications. Yet, there is limited understanding of how the native metabolism coordinates phenolic carbon processing with cofactor generation. Here, we achieve quantitative understanding of this metabolic balance through a multi-omics investigation of *Pseudomonas putida* KT2440 grown on four common phenolic substrates: ferulate, *p*-coumarate, vanillate, and 4-hydroxybenzoate. Relative to succinate as a non-aromatic reference, proteomics data reveal >140-fold increase in proteins for transport and initial catabolism of each phenolic substrate, but metabolomics profiling reveals that bottleneck nodes in initial phenolic compound catabolism maintain more favorable cellular energy state. Up to 30-fold increase in pyruvate carboxylase and glyoxylate shunt proteins implies a metabolic remodeling confirmed by kinetic ^{13}C-metabolomics. Quantitative analysis by ^{13}C-fluxomics demonstrates coupling of this remodeling with cofactor production. Specifically, anaplerotic carbon recycling via pyruvate carboxylase promotes fluxes in the tricarboxylic acid cycle to provide 50-60% NADPH yield and 60-80% NADH yield, resulting in 2-fold higher ATP yield than for succinate metabolism; the glyoxylate shunt sustains cataplerotic flux through malic enzyme for the remaining NADPH yield. The quantitative blueprint elucidated here explains deficient versus sufficient cofactor rebalancing during manipulations of key metabolic nodes in lignin valorization.

Lignin, a structural polymer in plant biomass that is considered the second most abundant biopolymer after cellulose, represents an important renewable carbon source[1]. Chemical depolymerization of lignin yields various phenolic compounds, which can be used directly as platform chemicals or as feedstocks for bioproduction[2–8]. Lignin-related phenolic structures include hydroxybenzoates (4-hydroxybenzoate, vanillate, gallate, and syringate) and hydroxycinnamates (*p*-coumarate and ferulate)[9]. Soil *Pseudomonas* species have native metabolic capabilities to process benzoate, 4-hydroxybenzoate (4HB), vanillate (VAN), gallate, *p*-coumarate (COU), and ferulate (FER)[10–18]. Of particular interest is *Pseudomonas putida* KT2440,

39   which is extensively explored as a chassis for biotechnology[19–22]. Encoded in *P. putida* KT2440 are

40   pathways for the catabolism of hydroxybenzoates and hydroxycinnamates involving *ortho*-cleavage of the

41   intermediate protocatechuate (PCA) through β-ketoadipate to generate carbon influx into the tricarboxylic

42   acid (TCA) cycle in the central carbon metabolism[13] (Fig. 1A). In the peripheral pathways upstream of β-

43   ketoadipate, the uptake and catabolism of hydroxycinnamates (COU and FER) and hydroxybenzoates

44   (4HB and VAN) to PCA are catalyzed by a series of enzymes with distinct cofactor specificities[13,23–28] (Fig.

45   1A). Previous metabolic engineering of *P. putida* targeted directing carbon influx from phenolic carbons

46   from initial catabolism towards desired products such as PCA, vanillin, β-ketoadipate, muconic acid,

47   pyridine 2,4-dicarboxylic acid, adipic acid, indigoidine, and polyhydroxyalkanoates[29–42]. Metabolic

48   bottlenecks, which were inferred from extracellular accumulation of VAN in FER-fed cells or of 4HB in

49   COU-fed cells[33,40,41,43–45], could not be overcome completely via genetic engineering due to cofactor

50   deficiency[33,43,41]. Therefore, metabolic engineering to enhance phenolic carbon conversion must address

51   appropriate cofactor supply. However, largely lacking is a quantitative understanding of how the native

52   metabolic network in *P. putida* KT2440 couples carbon fluxes from phenolic acid structures with cofactor
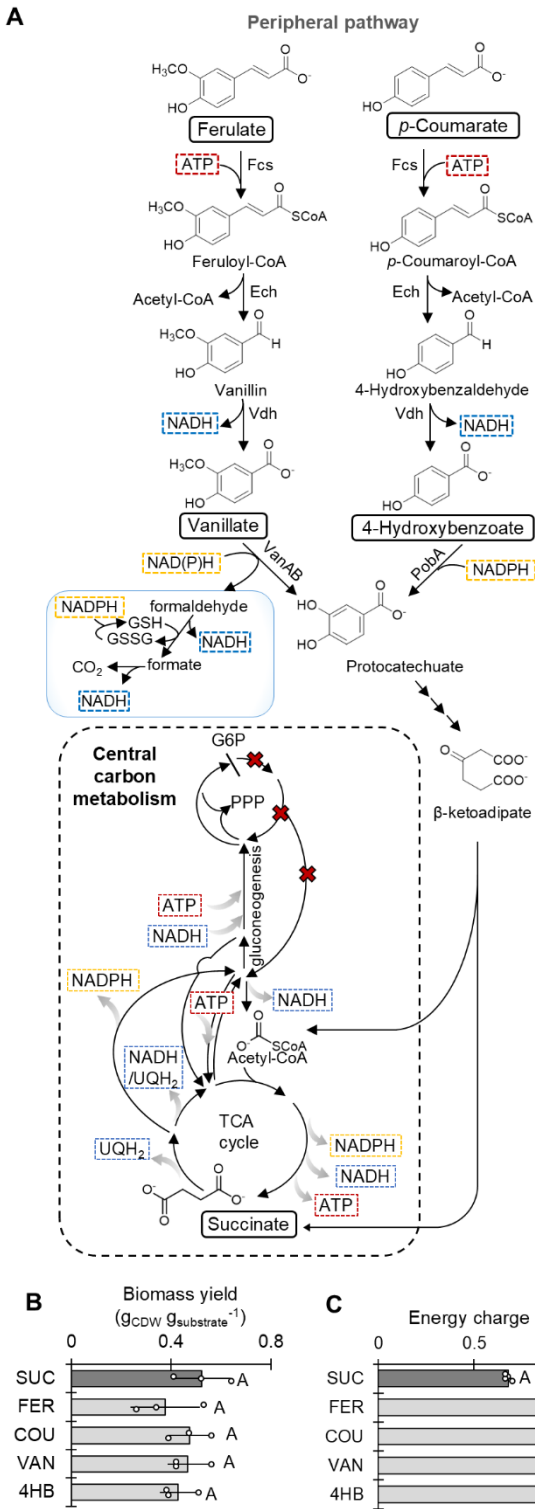
53   production.

54   Metabolic flux modeling or fluxomics constrained by ^{13}C-metabolomics data provides quantitative

55   analysis of carbon fluxes[46–53]. Previous ^{13}C-fluxomics studies of *P. putida* focused on glycolytic metabolism

56   for sugars (i.e., glucose, xylose) or gluconeogenic metabolism for succinate (SUC)[18,54–63]. The only two

57   fluxomics studies of aromatic carbon metabolism in *P. putida*, for benzoate alone or with glucose as a co-

58   substrate[17,18], both illustrated the activation of the glyoxylate shunt, which conserved carbon by

59   channeling isocitrate away from the canonical decarboxylation steps in the TCA cycle. Flux through the

60   glyoxylate shunt can feed into malic enzyme for NADPH generation, or malate dehydrogenase, for NADH

61   or ubiquinol generation. Interestingly, the flux through malate dehydrogenase was either 3-fold higher

62   than the flux through malic enzyme or there was only flux through malate dehydrogenase, both of which

63   would be advantageous to satisfy the NADH demand for benzoate catabolism through the catechol

64   pathway in *P. putida*[17,18]. For the catabolism of hydroxybenzoate and hydroxycinnamate structures, which

65   is funneled through PCA instead of catechol, it remains unknown how metabolic fluxes would be

66   partitioned in *P. putida* to optimize the catabolic pathways with cofactor supply (Fig. 1A).

67   While ATP in aerobic bacteria is generated primarily through oxidative phosphorylation of NADH

68   produced in glycolysis and the TCA cycle[64,65], the supply of NADPH required for biosynthesis and stress

69   tolerance is produced from different metabolic routes. During growth on glucose, NADPH production in *P.*

70   *putida* is mainly through glucose-6-phosphate dehydrogenase and 6-phosphogluconate dehydrogenase

71   in the oxidative pentose phosphate pathway (oxPPP)[56,59]. However, minimal to no flux in oxPPP was

72   reported during growth on two gluconeogenic substrates (SUC or benzoate)[17,60]. Instead, SUC

73   metabolism in *P. putida* relied on high flux through isocitrate dehydrogenase and malic enzyme in the TCA

74   cycle to produce NADPH, and on transhydrogenase reactions to replenish NADPH from excess NADH

75   pool[60]. Whether *P. putida* would rely on similar metabolic routing or energetic bypass for NADPH

76   production during phenolic substrate utilization remains to be elucidated.

77   The cataplerotic and anaplerotic nodes, which distribute respectively carbon fluxes from the TCA

78   cycle to gluconeogenesis and from lower glycolysis to the TCA cycle[66], have implications for cofactor

79   balance (Fig. 1A). In the cataplerotic direction, due to lack of phosphoenolpyruvate (PEP) carboxykinase

80   for the decarboxylation of oxaloacetate (OAA) to PEP[67], *P. putida* KT2440 must rely on either malic

81   enzyme to convert malate to pyruvate with NADPH production or OAA decarboxylase to convert OAA to

82   pyruvate with no cofactor involved[68]. In the anaplerotic direction, pyruvate carboxylation to OAA

83   consumes ATP, while PEP carboxylation to OAA has no cofactor input[68]. It remains unclear how *P. putida*

84   KT2440 would modulate carbon flux distribution between cataplerosis and anaplerosis to meet the

85   demand for reducing equivalents and energy required for phenolic carbon catabolism.

86   Here, our central hypothesis was that remodeling of carbon flux into and within the TCA cycle by *P.*

87   *putida* KT2440 would promote the net production of NAD(P)H and ATP to satisfy the cofactor demands in

88   the *p*-coumaroyl and coniferyl pathways (Fig. 1A). We tested our hypothesis by employing genetic

89   engineering, targeted metabolomics, whole-cell proteomics, kinetic ^{13}C-metabolomics, and ^{13}C-fluxomics

90   during feeding of *P. putida* KT2440 on FER, COU, VAN, or 4HB. First, using quantitative metabolomics for

91   cofactor profiling in wild-type and engineered strains, we investigated how the cellular energy state would

92   be influenced by alterations in the aromatic carbon influx in several strains that overexpressed key

93   bottleneck-relevant genes. Second, to construct the metabolic network that establishes the cellular

94   energy state, we profiled protein levels to identify metabolic remodeling nodes and verify these nodes

95   using kinetic ^{13}C-profiling in metabolites coupled with ^{13}C-carbon mapping. Third, we integrated the

96   proteomics and ^{13}C-metabolomics data to perform ^{13}C-fluxomics to map quantitatively carbon fluxes

97   through the metabolic network. Fourth, we leveraged the quantitative flux analysis to determine

98   production and consumption rates of cofactors, thereby evaluating metabolic flux controls on cofactor

99   maintenance during conversion of the different lignin-derived phenolic compounds. Our findings provide

100   quantitative insights into the relationship between carbon metabolism and energy metabolism in *P. putida*

101   KT2440 utilizing different hydroxycinnamate and hydroxybenzoate substrates related to lignin.

Fig. 1. Favorable energy charge from the metabolism of phenolic acid structures. (A) Schematic illustration of cofactor investment and production in the peripheral pathway and central carbon metabolism. (B) Biomass yield of *P. putida* cells utilizing SUC, FER, COU, VAN, and 4HB. Data are expressed as mean ± standard deviation from three biological replicates ($n = 3$). (C) Energy charge calculated from quantified ATP, ADP, and AMP pools when *P. putida* cells were fed with SUC, FER, COU, VAN, and 4HB. Energy charge = ([ATP] + 0.5 × [ADP]) / ([ATP] + [ADP] + [AMP]). Data are expressed as mean ± standard deviation from four independent biological replicates ($n = 4$). In B and C, data for SUC-fed condition were adapted from Wilkes et al.[60] Abbreviations: GSH, glutathione; GSSG, glutathione disulfide. The red crosses represent no carbon flux through the oxPPP and Entner–Doudoroff pathway during gluconeogenesis.

4

111 In B and C, one-way analysis of variance (ANOVA) was performed followed by Tukey's HSD post hoc test. Statistically
112 significant differences ($P < 0.05$) are denoted by a change in letter.

113

114 **Results**

115 **Bottleneck Nodes in Initial Phenolic Substrate Catabolism Sustain Favorable Cellular Energy**

116 **Balance.** During growth on 100 mM C of FER, COU, VAN or 4HB as the sole carbon source, *P. putida*

117 KT2440 showed growth rates ranging from 0.53-0.88 h^{-1} [Supplementary Information (SI), Fig. S1A],

118 which were 10-41% slower compared to growth rate reported for SUC[60], a non-aromatic substrate

119 reference. Substrate depletion rates were comparable for SUC and 4HB (16.0 ± 2.0 and 15.9 ± 3.1 mmol

120 g_{CDW}^{-1} h^{-1}, respectively) ($P = 0.96$), but the corresponding rates for FER, COU, and VAN were 58%, 38%,

121 and 49% lower than SUC, respectively ($P < 0.05$) (SI, Fig. S1B). Despite the differences in growth and

122 substrate depletion rates, the biomass yield of *P. putida* was similar across all five substrates ($P = 0.64$-

123 0.99) (Fig. 1B). Since biomass synthesis requires energy input, we further evaluated the energy status of

124 *P. putida* during feeding on the different substrates by calculating the energy charge using quantified

125 intracellular levels of ATP, ADP, and AMP[60] (SI, Table S1). Remarkably, we obtained 25-31% higher energy

126 charge when cells were fed on the phenolic substrates compared to SUC feeding ($P < 0.001$) (Fig. 1C; SI,

127 Table S1). These data implied that carbon influx during phenolic acid assimilation was optimized for

128 favorable cellular energy charge.

129 With respect to regulation of carbon influx, bottlenecks were proposed at three nodes in initial

130 phenolic acid catabolism, based on extracellular metabolic overflow in exponentially growing cells: the

131 VanAB node in the coniferyl branch[33,40], the PobA node in the *p*-coumaroyl branch[33,41,43], and the PcaHG

132 node downstream of both branches[40] (Fig. 1A). Here, we obtained direct evidence using intracellular

133 metabolomics analysis and ^{13}C kinetic isotopic profiling of exponentially growing cells to confirm the three

134 reported bottlenecks, in addition to identifying one at the Vdh node (Fig. 2). We evaluated changes in

135 cellular energy charge due to resolving the bottlenecks with gene overexpression (Fig. 2).

136 In the coniferyl branch, bottleneck at the Vdh node was characterized by vanillin accumulation (4.3 ±

137 0.5 µmol g_{CDW}^{-1}) relative to both the precursor feruloyl-CoA (0.2 ± 0.03 µmol g_{CDW}^{-1}) and the downstream

138 metabolites vanillate (1.1 ± 0.2 µmol g_{CDW}^{-1}) and PCA (below the detection limit) (Fig. 2A). This bottleneck

139 was further illustrated by 50% lower incorporation of ^{13}C-FER in vanillin compared to feruloyl-CoA within 1

140 min of isotope switch ($P < 0.05$) (Fig. 2B). Overexpression of *vdh* (strain RW127) led to an 80% decrease

141 in vanillin and a 24-fold increase in VAN ($P < 0.001$), indicating that addressing the bottleneck at Vdh

142 triggered a downstream bottleneck at VanAB (Fig. 2C). Even with VAN as the direct carbon source, PCA

143 level remained low (0.8 ± 0.1 µmol g_{CDW}^{-1}), due to inefficient VAN conversion by VanAB (Fig. 2C). In

144 relation to this bottleneck, we constructed three strains: RW124 with *vanAB* overexpression, RW125 with

145 combined overexpression of *vanAB* and *pcaHG*, and RW126 with stacked overexpression of *vdh*, *vanAB,*

146 *and pcaHG* (Fig. 2B). Compared to metabolite levels in RW127 fed on FER, a decreased VAN level (by

147 93%, $P < 0.001$) in RW126 indicated simultaneous alleviation of the bottlenecks at both Vdh and VanAB

148 (Fig. 2C). Compared to the wild-type strain grown on VAN, lack of PCA accumulation in RW124 and

149 depletion of PCA (by 83%, $P < 0.001$) in RW125 demonstrated efficient PCA cleavage and thus

150 elimination of the bottleneck at PcaHG during VAN catabolism (Fig. 2D). Cellular energy charge was 25-

151 44% lower in the mutant strains in the coniferyl branch compared to the wild-type strain ($P < 0.05$) (Figs.

152 2D, 2E; SI, Table S1).

153   In the *p*-coumaroyl branch, in line with the reported bottleneck node at PobA[33,41,43], there was 4HB

154 accumulation (18.1 ± 7.6 µmol g_{CDW}^{-1}) during COU catabolism, while 4-hydroxybenzaldehyde (4HBA) level

155 was 67% lower ($P < 0.05$) and PCA level was below the detection limit (Fig. 2F). Furthermore, in relation to

156 the bottleneck, there was 31% smaller fraction of ^{13}C-COU carbons in 4HB than in 4HBA within 1 min ($P <$

157 0.01) (Fig. 2G). During growth on 4HB, PCA accumulated (19.8 ± 5.4 µmol g_{CDW}^{-1}), in accordance with the

158 reported bottleneck at PcaHG (Fig. 2F)[40]. We prepared three strains that overexpressed either *pobA*

159 (RW128), *pcaHG* (RW123), or both *pobA* and *pcaHG* (RW129) (Fig 2H). Compared to the wild-type strain,

160 the bottlenecks were resolved in RW128 and RW123, characterized by a 90% decrease in 4HB during

161 growth on COU and a 50% decrease in PCA during growth on 4HB ($P < 0.05$), respectively (Figs. 2I, 2J).

162 Similar to the coniferyl branch, the energy charge of the mutants of the *p*-coumaroyl branch was 32-40%

163 lower than in the wild-type stain ($P < 0.05$) (Fig. 2I, 2J; SI, Table S1).

164   In sum, alleviation of native metabolite buildups in initial substrate catabolism led to adverse change in

165 the cellular energy charge, thereby implying an interplay between the regulation of phenolic carbon influx

166 and cofactor balance and a potential energy burden caused by gene overexpression[62]. Towards

167 understanding the metabolic mechanisms underlying native cofactor balance, we investigated protein

168 levels, metabolite pools, and the network of carbon fluxes during processing of the different phenolic

169 compounds.

170
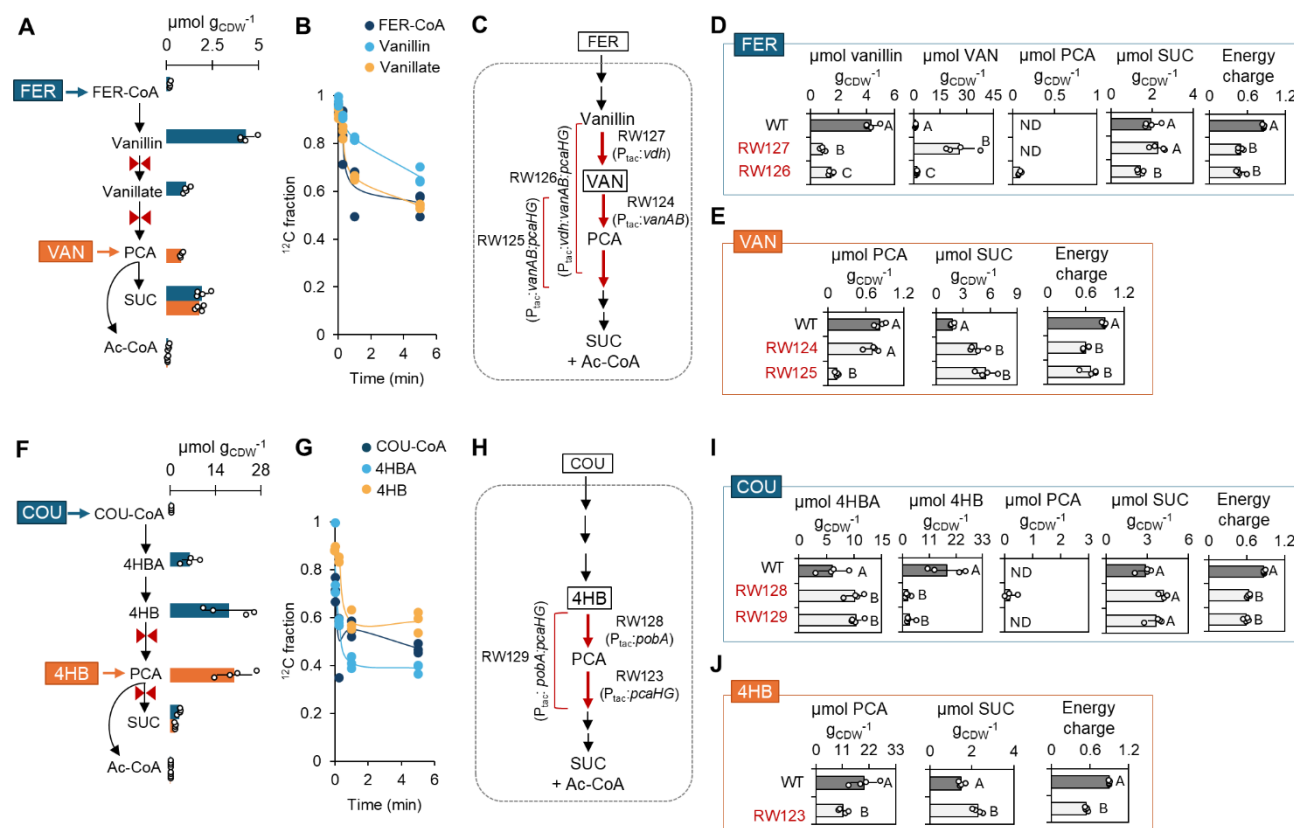
171
172 **Fig. 2. Intracellular evidence of bottleneck nodes in the peripheral pathways of phenolic substrate catabolism.**
173 (A) Intracellular levels of intermediates involved in FER and VAN utilization. (B) Kinetic depletion in unlabeled (^{12}C)
174 fraction of key metabolites in the coniferyl branch during incorporation of ^{13}C-FER. (C) Targeted nodes in the coniferyl
175 branch for gene overexpression. Intracellular metabolite levels and energy charge in the wild-type and mutant strains
176 during feeding on (D) FER and (E) VAN. (F) Intracellular levels of intermediates involved in COU and 4HB utilization
177 by *P. putida*. (G) Kinetic depletion in the unlabeled (^{12}C) fraction of key metabolites in the *p*-coumaroyl branch during
178 incorporation of ^{13}C-COU. (H) Targeted nodes in the *p*-coumaroyl branch for gene overexpression. Intracellular
179 metabolite levels and energy charge in the wild-type and mutant strains during feeding on (I) COU and (J) 4HB. In B
180 and F, red bowties indicate the identified bottlenecks. ND: not detected. Abbreviations: FER-CoA, feruloyl-CoA; COU-
181 CoA, *p*-coumaroyl-CoA. In D, E, and I, one-way ANOVA was performed followed by Tukey's HSD post hoc test to
182 determine the significance. In J, unpaired *t*-test was performed to evaluate the significance. Statistically significant
183 differences ($P < 0.05$) are denoted by a change in letter. All data in A, D, E, F, I, and J are obtained from four
184 independent biological replicates ($n = 4$). All data in B and G were obtained from three independent biological replicates
185 ($n = 3$).

186 **Abundances of Transporters and Specialized Enzymes Are Modulated to Adapt to Phenolic Carbon**
187 **Influx.** For each of the four biological replicates, we employed a high-resolution proteomics method to
188 capture over 4300 proteins out of the 5950 total proteins encoded by *P. putida* KT2440, including low-
189 abundance proteins that are typically undetected (SI, Table S2)*.* From whole-cell proteomics analysis of *P.*
190 *putida* cells fed on each phenolic substrate compared to cells fed on SUC, we profiled statistically significant
191 changes ($P < 0.05$) in the abundance of proteins involved in membrane transport, the coniferyl branch, the
192 *p*-coumaroyl branch, and the central carbon metabolism (Fig. 3 and Fig. 4). The HcnK abundance was 700-
193 fold greater in *P. putida* cells fed with FER or COU (Fig. 3A), in agreement with the assignment of HcnK as
194 the common transporter for hydroxycinnamate uptake to both the coniferyl and *p*-coumaroyl branches[27].
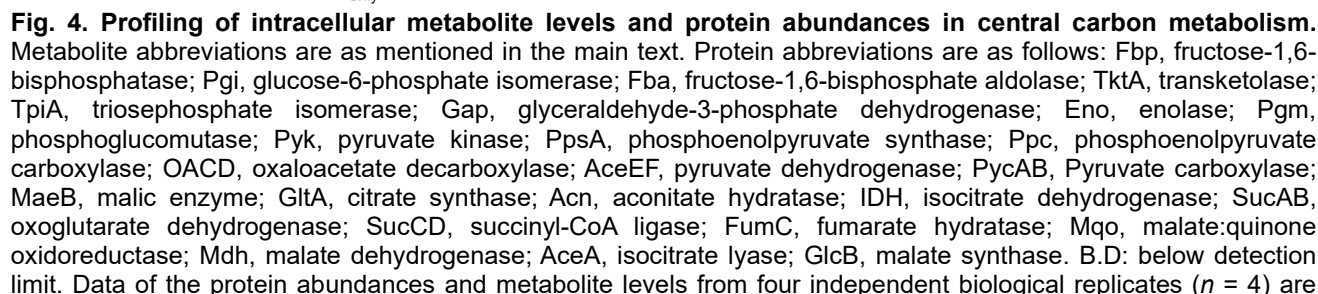
195   However, HcnK abundance was also 9-fold to 13-fold higher in cells grown on VAN and 4HB relative to SUC

196   (Fig. 3A; SI, Table S3), indicating that abundance of this transporter was also induced by downstream

197   metabolites in the pathways. For the VAN transporter VanK[27], its abundance was 830-fold higher in cells fed

198   with VAN or FER compared to SUC (Fig. 3A; SI, Table S3), indicating the dependence of VanK level on the

199   presence of VAN either as a substrate or as an intermediate in FER catabolism (Fig. 1A). Similarly, the

200   abundance of 4HB transporter PcaK was increased to similar extent (> 140-fold) during growth across all

201   four phenolic substrates compared to growth on SUC, in accordance with PcaK serving also as a

202   transporter of PCA[26,27,69], a common downstream intermediate in both the coniferyl and p-coumaroyl

203   branches (Fig. 3A; SI, Table S3).

204   After substrate uptake, a series of cofactor-dependent enzymes are involved in the initial catabolism

205   (Fig. 3A). Compared to SUC-fed cells, the abundances of Fcs, Ech, and Vdh, which collectively catalyze

206   the conversion of FER to VAN or COU to 4HB, were up to 590-fold higher in cells fed on FER or COU, but

207   remained unchanged in cells grown on VAN or 4HB (Fig. 3A; SI, Table S3). The abundance of VanAB,

208   which catalyze VAN O-demethylation to produce PCA and formaldehyde, was up to 2700-fold higher in

209   cells grown on FER or VAN compared to SUC; the corresponding increase during feeding on COU and

210   4HB was 60-fold (Fig. 3A; SI, Table S3). To avoid the accumulation of toxic formaldehyde, $P. putida$ can

211   oxidize formaldehyde to CO_2 via formate as an intermediate using formaldehyde dehydrogenase (FrmA,

212   FdhA) and formate dehydrogenase (Fdh, Fmd, Fdo) (Fig. 3B)[70,71]. Accordingly, relative to SUC-grown cells,

213   the abundance of FrmA and FdhD was up to 40-fold higher in cells grown on FER or VAN, but remained

214   unchanged in cells grown on COU or 4HB (Fig. 3B). Related to stress tolerance strategies[72,73], abundance

215   of TtgABC efflux pump was 3-fold higher in VAN-grown cells compared to SUC-fed cells (SI, Table S3),

216   suggesting its involvement in formaldehyde tolerance. For the conversion of 4HB to PCA, the abundance

217   of PobA was up to 3100-fold higher during feeding on COU or 4HB relative to SUC feeding; the

218   corresponding change was up to 550-fold higher in cells grown on FER or VAN (Fig. 3A; SI, Table S3).

219   Taken together, the increased abundance of the initial catabolic enzymes across all substrates

220   implied co-regulation in the utilization of the different phenolic substrates. In fact, compared to growth on

221   SUC, the levels of enzymes (PcaHGBCDJIF) involved in the $ortho$-cleavage of PCA via the β-ketoadipate

222   pathway showed 40-fold to 500-fold increase during growth on the four phenolic substrates (Fig. 3A; SI,

223   Table S3). Notably, the β-ketoadipate pathway generates SUC and acetyl-CoA as additional carbon

224   influxes into the TCA cycle compared to metabolism of SUC alone (Fig. 3A). Next, we evaluated changes

225   in both protein abundances and intracellular metabolite levels in the central carbon metabolism (Fig. 4).
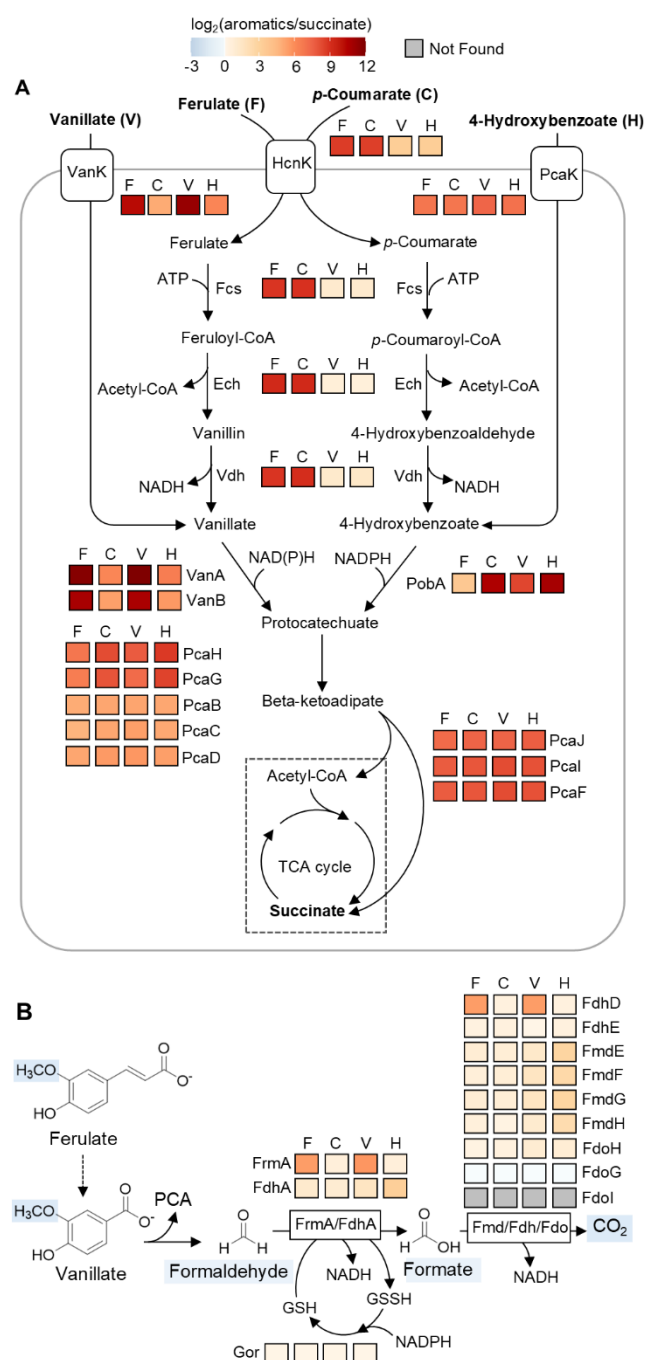
226
Fig. 3. Profiling protein abundance changes in the peripheral pathways. Log2 fold change in protein abundance in (A) the peripheral pathways and (B) formaldehyde oxidation pathway. Abbreviation of enzymes: HcnK, hydroxycinnamic acid transporter; VanK, vanillate transporter; PcaK, 4-hydroxybenzoate/protocatechuate transporter; Fcs, feruloyl-CoA synthase; Ech, feruloyl-CoA hydratase-lyase; Vdh, vanillin dehydrogenase; VanAB, vanillate O-demethylase; PobA, 4-hydroxybenzoate 3-monooxygenase; PcaH, protocatechuate 3,4-dioxygenase beta chain; PcaG, protocatechuate 3,4-dioxygenase alpha chain; PcaC, 4-carboxymuconolactone decarboxylase; PcaB, 3-carboxy-cis,cis-muconate cycloisomerase; PcaD, 3-oxoadipate enol-lactonase; PcaIJ, 3-oxoadipate CoA-transferase; PcaF, betaketoadipyl-CoA thiolase; FrmA, formaldehyde dehydrogenase; FdhA, formaldehyde dehydrogenase; FmdEFGH, formate dehydrogenase; FdhDE, formate dehydrogenase; FdoHGI, formate dehydrogenase; Gor, glutathione reductase. Log2 fold change and *P* values are provided in SI, Table S3, using data obtained from four independent biological replicates (*n* = 4). The full dataset of proteomics is provided in Supplemental Dataset 1.

9

Fig. 4. Profiling of intracellular metabolite levels and protein abundances in central carbon metabolism. Metabolite abbreviations are as mentioned in the main text. Protein abbreviations are as follows: Fbp, fructose-1,6-bisphosphatase; Pgi, glucose-6-phosphate isomerase; Fba, fructose-1,6-bisphosphate aldolase; TktA, transketolase; TpiA, triosephosphate isomerase; Gap, glyceraldehyde-3-phosphate dehydrogenase; Eno, enolase; Pgm, phosphoglucomutase; Pyk, pyruvate kinase; PpsA, phosphoenolpyruvate synthase; Ppc, phosphoenolpyruvate carboxylase; OACD, oxaloacetate decarboxylase; AceEF, pyruvate dehydrogenase; PycAB, Pyruvate carboxylase; MaeB, malic enzyme; GltA, citrate synthase; Acn, aconitate hydratase; IDH, isocitrate dehydrogenase; SucAB, oxoglutarate dehydrogenase; SucCD, succinyl-CoA ligase; FumC, fumarate hydratase; Mqo, malate:quinone oxidoreductase; Mdh, malate dehydrogenase; AceA, isocitrate lyase; GlcB, malate synthase. B.D: below detection limit. Data of the protein abundances and metabolite levels from four independent biological replicates (*n* = 4) are

10

250　provided in SI, Tables S3 and S4. The full dataset of proteomics is provided in Supplemental Dataset 1.

251　**Fluxes through β-Ketoadipate Pathway and Enhanced Anaplerosis Promote Carbon Retention in the**

252　**TCA Cycle.** During phenolic substrate utilization, malate decreased by up to 70% ($P < 0.05$), while PEP

253　and 3-phosphoglycerate (3PG) increased 2-fold to 60-fold ($P < 0.01$) relative to SUC utilization, indicating

254　strong cataplerotic flux from the TCA cycle towards intermediates in gluconeogenesis (Fig. 4; SI, Table

255　S4). By contrast, citrate (CIT) and alpha-ketoglutarate (AKG) levels were up to 10-fold and 7-fold higher (P

256　< 0.001), respectively, in cells grown on phenolic substrates than on SUC, implying high carbon flux

257　towards the high energy-producing side of the TCA cycle (Fig. 4; SI, Table S4). Despite these changes in

258　metabolite levels, only three nodes in central carbon metabolism showed greater than 2-fold changes in

259　protein abundance during growth on the phenolic substrates relative to growth on SUC. First, the enzyme

260　catalyzes the anaplerotic reaction of pyruvate carboxylation to OAA (Pyc) was 2.5-fold to 6-fold more

261　abundant, but the abundance of Ppc, which catalyzes the other anaplerotic reaction of PEP carboxylation

262　remained mostly unchanged (< 2-fold), suggesting a dominant role of Pyc during growth on phenolic

263　compounds (Fig. 4; SI, Table S3). Second, the two enzymes (AceA and GlcB) involved in the glyoxylate

264　shunt were 2-fold to 30-fold more abundant (Fig. 4; SI, Table S3). Third, the abundance of AceE and AceF,

265　which catalyze pyruvate to acetyl-CoA, was up to 6-fold lower in cells fed on FER or COU, potentially due

266　to the acetyl-CoA surplus. Thus, the proteomics profiling implied an increased cataplerotic flux, activation

267　of the glyoxylate shunt, and a decreased flux in pyruvate dehydrogenase during phenolic catabolism. To

268　corroborate this inferred metabolic remodeling, we performed kinetic ^{13}C-profiling of *P. putida* KT2440

269　cells switched from unlabeled substrates to 50% phenyl-^{13}C$_6$-FER, phenyl-^{13}C$_6$-COU, phenyl-^{13}C$_6$-VAN,

270　phenyl-^{13}C$_6$-4HB, or U^{13}C$_4$-SUC (Fig. 5A).

271　　　　The kinetic ^{13}C-profiling of intracellular metabolites was aimed at capturing routing of substrate

272　carbons in specific metabolic pathways. After 1 min, the ^{13}C-labeled fractions of SUC were at up to 24% in

273　cells grown on FER and VAN, but at up to 52% in cells grown on COU and 4HB ($P < 0.001$) (Fig. 5B). The

274　slower incorporation of ^{13}C into the coniferyl branch relative to the *p*-coumaroyl branch was consistent

275　with up to 58% slower uptake rates of the respective substrates (SI, Fig. S1). The ^{13}C-labeled fraction of

276　acetyl-CoA in cells fed with the hydroxycinnamates (FER and COU) was up to 50% lower than in cells

277　grown on the hydroxybenzoates (VAN and 4HB) ($P < 0.05$), due to the production of unlabeled acetyl-CoA

278　via Ech (Fig. 5B). Further, consistent with the additional acetyl-CoA influx from the β-ketoadipate pathway,

279　^{13}C-labeled acetyl-CoA was predominantly doubly ^{13}C-labeled (> 90%) during growth on the phenolic

280　substrates (Fig. 5B). Under similar uptake rates, despite 3-fold to 30-fold higher CIT and aspartate (Asp)

281　levels in cells fed with 4HB compared to SUC ($P < 0.001$), ^{13}C-labeled fraction within 15 s was up to 2-fold

282　higher in 4HB-grown cells ($P < 0.01$), confirming exceptionally high TCA cycle flux for 4HB assimilation

283　(SI, Table S4; Figs. 5B).

284　　　　We further confirmed metabolic remodeling through carbon mapping combined with ^{13}C-

285　metabolomics (Figs. 5C, 5D, and 5E). First, regarding metabolic remodeling through anaplerosis inferred

286　from the change of Pyc abundance, we determined the relative fraction of OAA derived from pyruvate by

11

287   tracking triply ^{13}C-labeled OAA (via Asp labeling), which would be generated only from the carboxylation

288   of triply ^{13}C-labeled pyruvate by unlabeled CO_2 (Fig. 5C). At the plateau of the kinetic ^{13}C data, we

289   recorded 38% triply ^{13}C-labeled pyruvate and 6% triply ^{13}C-labeled Asp in the SUC-fed cells (Fig. 5B),

290   reflecting that 16% of OAA was derived from pyruvate (Fig. 5C), consistent with previous flux analysis[74].

291   However, the isotopologue profiling in cells fed on the phenolic substrates revealed 30% to 45% of OAA

292   derived from pyruvate (Fig. 5C), confirming the enhanced Pyc-catalyzed pyruvate carboxylation to OAA

293   (*i.e.*, anaplerosis) implied by the proteomics data.

294   Second, to verify metabolic remodeling through the glyoxylate shunt, we illustrated carbon mapping

295   for two scenarios. In one scenario, SUC generated exclusively through the canonical TCA cycle with no

296   flux through the glyoxylate shunt would result in non-labeled, singly ^{13}C-labeled, triply ^{13}C-labeled, and

297   fully ^{13}C-labeled SUC after one cycle of carbon mapping (Fig. 5D); an additional cycle would generate the

298   same isotopologues (SI, Fig. S3). In another scenario, the glyoxylate shunt in the TCA cycle would

299   generate doubly ^{13}C-labeled SUC through isocitrate lyase (AceA) (Fig. 5E). Detection of this doubly ^{13}C-

300   labeled isotopologue only in the cells fed on phenolic substrates confirmed the activation of the glyoxylate

301   shunt during the metabolism of these substrates (Fig. 5B). We performed ^{13}C-fluxomics to obtain

302   quantitative insights into the metabolic network remodeling.
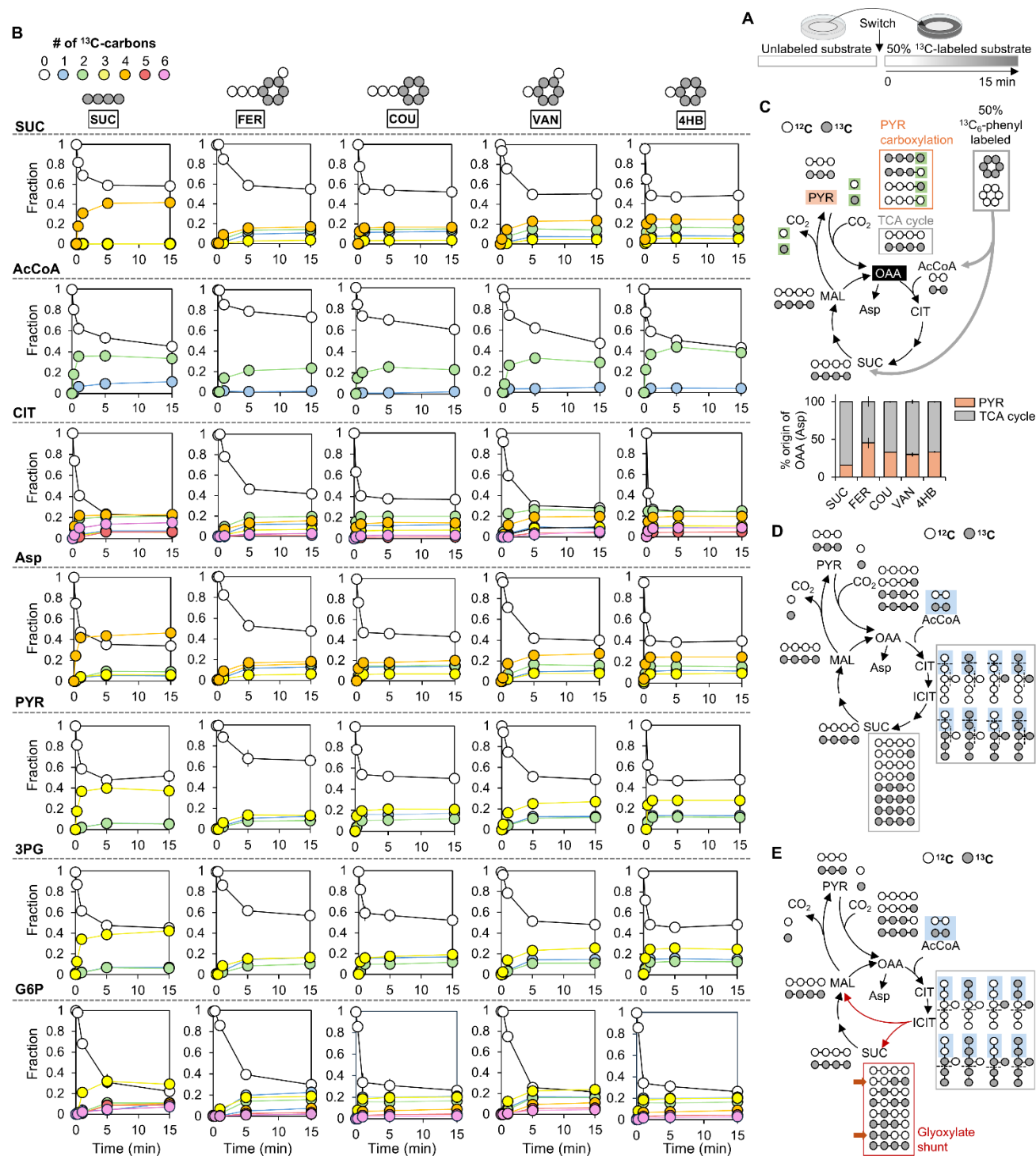
Fig. 5. Kinetic ^{13}C-profiling and carbon mapping of metabolites in the central carbon metabolism. (A) Schematic illustration of kinetic isotope incorporation experiment using 50% ^{13}C-labeled substrates. (B) Kinetic ^{13}C-profiling of central carbon metabolites. (C) Contribution from pyruvate versus malate to the oxaloacetate pool determined by carbon mapping when cells were grown on 50% ^{13}C-labeled phenolic substrates or SUC. Isotopologues of TCA cycle intermediates predicted by carbon mapping when assuming (D) 100% canonical TCA cycle and (E) 100% glyoxylate shunt. Kinetic ^{13}C-profiling of dihydroxyacetone phosphate, PEP, and sedoheptulose-7-phosphate are provided in SI, Fig. S4. For clarity, we presented the data in (B) as mean ± standard deviation from three independent biological replicates (n = 3), error bars are not visible where data across the three biological replicates were highly reproducible. Individual data points for kinetic ^{13}C-metabolomics are provided in Supplemental Dataset 2. Abbreviations of metabolites are the same as shown in the main text.

13

High flux retention in the TCA cycle sustains cofactor surplus. The algorithm for the ^{13}C-fluxomics of each of the four phenolic substrates was constrained by biomass growth rates, substrate depletion rates, metabolite secretion rates, intracellular metabolite levels, and kinetic ^{13}C-profiling of metabolites (Fig. 6A-6D). Relative to SUC metabolism, the β-ketoadipate pathway provides an additional influx of acetyl-CoA from the phenolic substrates and the presence of the acryl group in the hydroxycinnamates generates a surplus acetyl-CoA (Fig. 1A). Consequently, we obtained 2-fold to 9-fold increase in carbon fluxes in the TCA cycle during phenolic catabolism compared to SUC utilization (Figs. 6A-6D; SI, Fig. S5). Moreover, the citrate synthase flux, which combines OAA with acetyl-CoA to form CIT, was up to 2-fold higher for the catabolism of the hydroxycinnamate compounds (FER and COU) than the hydroxybenzoate compounds (VAN and 4HB) (Figs. 6A-6D). Accordingly, flux through the glyoxylate shunt was determined to be 2.5-fold to 13-fold higher during metabolism of the hydroxycinnamates than the hydroxybenzoates (Figs. 6A-6D). This flux difference with the different phenolic compounds was consistent with our proteomics data on the relative abundance of AceA in the glyoxylate shunt (Fig. 4; SI, Table S3).

With respect to the flux remodeling at the cataplerosis-anaplerosis nodes, the cataplerotic flux through malic enzyme was 1.4-fold to 2.5-fold higher during phenolic substrate catabolism compared to SUC catabolism, while there was no flux through OAA decarboxylase (Figs. 6A-6D; SI, Fig. S5). Informed by the proteomics data, which highlighted up to 6-fold increase in Pyc (pyruvate carboxylase) relative to less than 2-fold increase in Ppc (PEP carboxylase) ($P < 0.001$), anaplerotic flux was constrained to occur only via Pyc, involving the carboxylation of pyruvate to OAA, to replenish four-carbon intermediates in the TCA cycle (Fig. 4). This pyruvate-to-OAA anaplerotic flux was 7-fold to 20-fold higher during phenolic substrate utilization than SUC utilization (Figs. 6A-6D; SI, Fig. S5), in agreement with the 2-fold to 3-fold higher OAA production from pyruvate influx illustrated by the carbon mapping combined with kinetic ^{13}C-metabolomics (Fig. 5C).

For resolving whether to include flux through pyruvate dehydrogenase, we performed ^{13}C-fluxomics with and without the reaction of pyruvate to acetyl-CoA (SI, Table S5). The model fit was not statistically acceptable when we deactivated the reaction in FER and COU (SI, Table S5). Therefore, pyruvate dehydrogenase was thus considered active during the phenolic substrate catabolism despite the observed decrease in the protein abundance (Fig. 4), suggesting possible sufficient abundance to support flux or post-translational regulation[18,75].

When we compared our high-resolution ^{13}C-fluxomics of the metabolic network with the widely used approach of flux balance analysis (FBA), both revealed that sustenance of high TCA cycle flux was prioritized over gluconeogenic flux during phenolic substrate catabolism (Figs. 6A-6D; Supplemental Dataset 4). Specifically, the ^{13}C-fluxomics predicted that only 13-16% of the cataplerotic flux from the TCA cycle to pyruvate was invested towards gluconeogenic flux, while 69-77% was recycled back to the TCA cycle via both pyruvate carboxylase (to replenish OAA) and pyruvate dehydrogenase (to generate acetyl-CoA) (Figs. 6A- 6D). The FBA still predicted 78-86% of carbon retention in the TCA cycle but indicated low cataplerotic flux through malic enzyme (14-22%) instead of the anaplerotic carbon recycling predicted

14

351   by the ^{13}C-fluxomics, a difference that we attributed to the low resolution of the anaplerosis-cataplerosis

352   node in the FBA algorithm (Supplemental Dataset 4).

353   With respect to relationships between our ^{13}C-fluxomics and proteomics data, there was a general

354   trend of positive correlation between changes in protein abundances and changes in fluxes in

355   cataplerosis, anaplerosis, 4 reactions in gluconeogenesis, and at least 7 reactions in the TCA cycle (Fig.

356   6E). Due to the discrepant magnitudes in the respective protein abundance and flux changes, there was

357   an overall poor correlation between the relative changes in the metabolic fluxes versus changes in protein

358   abundances (Pearson correlation, r = 0.11-0.35, P = 0.08-0.59) (Fig. 6E). Therefore, our correlation

359   matrices are consistent with the proposal that metabolic fluxes in central carbon metabolism are driven

360   primarily by thermodynamic factors and post-translational modifications[18,75].

361   To examine consequences of the remodeled metabolic network on cofactor balance, we determined

362   the rates of production and consumption of NADPH, NADH/UQH$_2$, and ATP during the catabolism of the

363   phenolic substrates compared to SUC, as a reference (Figs. 7A and 7B). Increased flux through

364   cataplerosis via malic enzyme and through isocitrate dehydrogenase in the TCA cycle led to 1.2-fold to

365   2.5-fold greater NADPH production in cells grown on phenolic substrates compared to SUC-grown cells

366   (Fig. 7B). As a result, the NADPH production was 24%-44% in excess of the NADPH demand for biomass

367   synthesis and the peripheral pathway including formaldehyde detoxification; this NADPH surplus was

368   routed to NADH synthesis through transhydrogenase reactions (Fig. 7B). Due to the promoted retention of

369   carbon flux in the TCA cycle, NADH/UQH$_2$ production was 1.4-fold to 2.7-fold higher during catabolism of

370   phenolic substrates relative to SUC utilization (Fig. 7B). The NADH surplus was 1.4-fold to 2.7-fold higher

371   in phenolic substrate-fed cells than SUC-grown cells, resulting in a corresponding fold increase in ATP

372   production via oxidative phosphorylation (Fig. 7B). In corroboration of the model-predicted ATP surplus,

373   absolute quantitation of the cellular ATP content revealed up to 2-fold higher ATP in cells fed with FER,

374   COU, or 4HB than in the SUC-fed cells (P <0.01) (Fig. 7C). The surplus of ATP was consistent with the

375   relatively higher energy charge values during processing of the phenolic substrates compared to SUC

376   (Fig. 1C), underscoring the optimization of the carbon metabolism in *P. putida* to maintain a high-energy

377   state during phenolic substrate utilization.
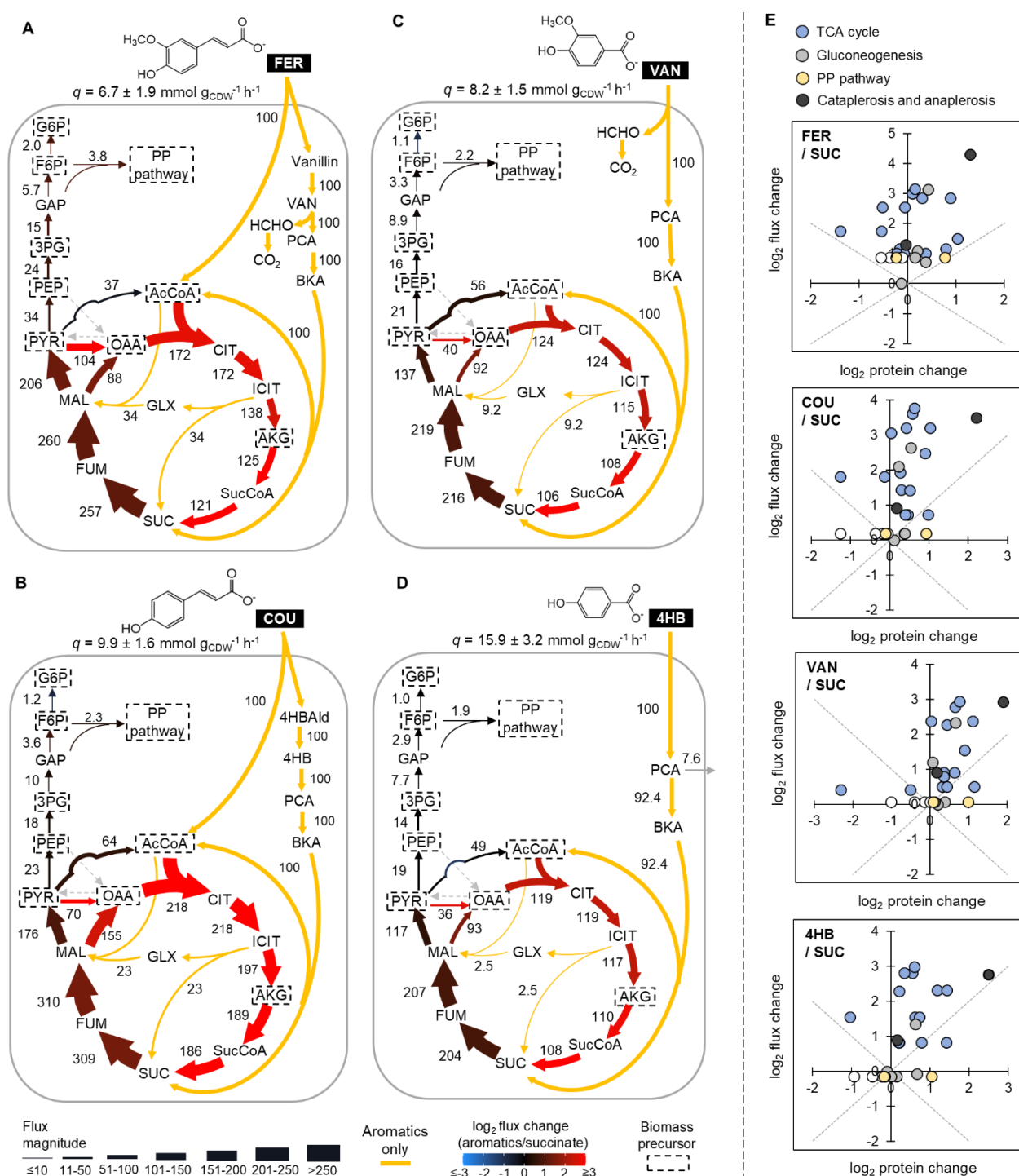
Fig. 6. Quantitative flux analysis of phenolic acid metabolism and correlation between ^{13}C-fluxomics and proteomics. Optimized flux model of *P. putida* KT2440 grown on (A) FER, (B) COU, (C) VAN, and (D) 4HB as the sole carbon source constrained by proteomics, metabolite pool sizes, and ^{13}C metabolomics data. (E) Correlation matrices of relative flux changes versus relative protein abundance changes. All fluxes are normalized to the substrate uptake rate (*q*). The weight of arrows is relative to flux magnitude. Relative flux changes between cells grown on the phenolic substrates and SUC are denoted by a red-black-blue color scheme. Increased flux is shown in shades of red, decreased flux is shown in shades of blue, and black indicates negligible differences in flux values. The yellow arrows represent fluxes that are predicted to be only in phenolic acid catabolism. The grey arrow represents metabolite secretion. Flux model of *P. putida* grown on SUC is provided in SI, Fig. S5. The complete flux estimations are provided in Supplemental Dataset 3. Abbreviations of metabolites are the same as shown in the main text.

16

389
390
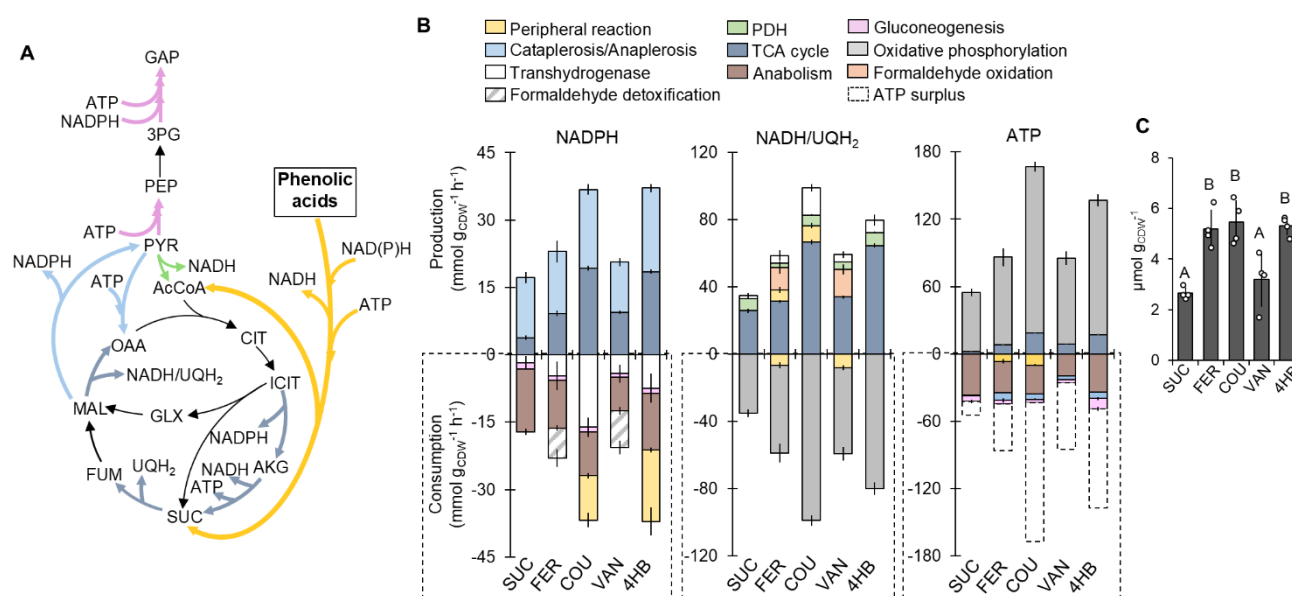
391
392 **Fig. 7. Cofactor balance in *P. putida* during carbon metabolism of the four lignin-derived phenolic substrates**
393 **compared to succinate.** A) Schematic illustration of metabolic reactions involving NADPH, NADH/UQH$_2$, and ATP.
394 (B) Production and consumption rates (mmol g$_{CDW}^{-1}$ h^{-1}) of NADPH, NADH/UQH$_2$, and ATP. Production of ATP from
395 NADH/UQH$_2$ was calculated using a phosphate to oxygen (P/O) ratio of 1.5. Abbreviations of metabolites are the same
396 as shown in the main text. (C) Quantified intracellular ATP pool size (µmol g$_{CDW}^{-1}$) in cells grown on the lignin-related
397 phenolic substrates compared to succinate. Data are expressed as mean ± standard deviation from four independent
398 biological replicates (*n* = 4). In C, one-way ANOVA was performed followed by Tukey's HSD post hoc test. Statistically
399 significant differences (*P* < 0.05) are denoted by a change in letter.

400

Discussion

401 The catabolism of lignin-derived phenolic substrates represents a critical step in valorizing lignin using

402 biotechnologically relevant microbes[2–7]. Strains of *P. putida* are extensively studied for this endeavor due

403 to their native ability to catabolize various aromatic compounds[10,11,13,14,16–18,37,76]. However, elucidation of

404 the native metabolic network in relation to cofactor balance in *P. putida* during catabolism of phenolic

405 substrates remains a knowledge gap. Here, we performed a comprehensive quantitative analysis of the

406 metabolic underpinnings of carbon and energy fluxes in *P. putida* KT2440 during conversion of two

407 hydroxycinnamates and two hydroxybenzoates, which represent common lignin-derived phenolic

408 substrates.

409 To address metabolic bottlenecks during conversion of phenolic substrates, increase in enzyme

410 expression was shown to be a successful strategy when an enzyme (i.e., VanA or VanB) exhibited a

411 preference for NADH over NADPH, but bottleneck was not alleviated for an enzyme (i.e., PobA) with

412 NADPH specificity due to cofactor deficiency[28,33,40,43]. The latter deficiency was circumvented by

413 substituting for an enzyme with broader cofactor specificity (i.e., PraI) or by increasing NADPH supply

414 through substrate co-feeding[41,43]. Our quantitative flux analysis determined that the metabolic fluxes

415 generated excess in both NADPH and NADH in *P. putida* KT2440, but the NADH surplus was up to 6-fold

416 higher than the NADPH surplus. Thus, our findings implied that the native cofactor balance was more

17

418   amenable to buffering increased NADH demand than increased NADPH demand from enzyme

419   overexpression.

420   Predicted by our proteomics data and confirmed by ^{13}C-fluxomics, we identified key nodes of flux

421   remodeling with important energetic consequences during the metabolism of the phenolic substrates. At

422   the cataplerosis-anaplerosis nexus between the TCA cycle and lower glycolysis, *P. putida* KT2440

423   exhibited the specific cataplerotic routing of carbon fluxes through malic enzyme (to deplete malate and

424   produce pyruvate) and anaplerotic routing through pyruvate carboxylase (to replenish OAA). This

425   adaptation of cataplerosis and anaplerosis generated 50% of the NADPH yield and sustained high flux

426   through the TCA cycle to produce over 70% of the NADH yield, which eventually fueled oxidative

427   phosphorylation for ATP production. A similar routing of carbon fluxes through the cataplerosis-

428   anaplerosis nodes was noted in glucose-grown *P. putida* to satisfy elevated cofactor demands in response

429   to oxidative and energetic stresses[18,59]. For instance, in response to oxidative stress, *P. putida* has been

430   shown to enhance carbon flux from glucose catabolism through the oxPPP to generate excess NADPH

431   that exceeded 50% of the biomass demand[59]. Moreover, when the conversion of NADH to ATP via

432   oxidative phosphorylation was uncoupled chemically in glucose-fed *P. putida*, there was an increase in

433   carbon flux through the high-energy producing side of the TCA cycle towards providing NAD(P)H and

434   ATP production to counterbalance the metabolic perturbation[54]. Thus, we propose that cofactor-driven

435   metabolic reprogramming is a widespread phenomenon under different substrate utilization.

436   The *ortho*-cleavage pathway, the only known catabolic route for the phenolic substrates in *P. putida*

437   (particularly strain KT2440), generates SUC and acetyl-CoA to feed into the TCA cycle. There are two

438   other reported aerobic PCA cleavage pathways: for example, the 2,3-*meta* cleavage pathway found in *P.*

439   *putida* strains mt-2 and H, and the 4,5-*meta* cleavage pathway revealed in *Comamonas testosteroni* and

440   *Sphingobium sp*. SYK-6[75,77–81]. The 2,3-*meta* cleavage route generates pyruvate and acetyl-CoA with the

441   production of NADH[78,81]; the 4,5-*meta* cleavage route generates OAA and pyruvate with the production of

442   NADPH[75,80]. The quantitative analysis employed here to decode cofactor balance involved in the *ortho*-

443   cleavage pathway could be used to evaluate the metabolic routing of phenolic carbons and cellular

444   cofactor balance following the other cleavage pathways.

445   Here we focused on the catabolism of hydroxycinnamates and hydroxybenzoates with PCA as the

446   common catabolic intermediate in *P. putida* KT2440. Lignin-derived compounds can constitute other

447   aromatic structures[9], with different intermediates such as catechol and gallate[10,13,17]. Moreover, sugar

448   monomers and aliphatic acids often co-exist with phenolic acids in hydrolysates of lignocellulosic

449   feedstocks[82,83]. Further investigation is needed to address the energy metabolism in *P. putida* during co-

450   utilization of different phenolic structures with or without sugars or aliphatic acids.

451   In sum, we unraveled interplay between carbon metabolism and energy metabolism in *P. putida* KT2440

452   grown on lignin-derived phenolic substrates, thus addressing the knowledge gap of quantitative flux analysis

453   during utilization of these substrates. Our findings provide a valuable quantitative blueprint of the native

454   metabolic network for further explorations of Pseudomonads and other related bacterial platforms for lignin

455   valorization.

Materials and Methods

Bacterial cultivation. *Pseudomonas putida* (strain KT2440) was obtained from the American Type Culture Collection (ATCC) and stored in Lysogeny broth (Miller) nutrient-rich medium with 25% glycerol at -80 °C. Cells were washed and inoculated from frozen stocks into 20-mL glass tubes that contained 5 mL of pH-adjusted (7.0) minimal nutrient medium with 100 mM C of ferulate (FER), *p*-coumarate (COU), vanillate (VAN), 4-hydroxybenzoate (4HB) or succinate (SUC) as the sole carbon source. The minimal nutrient medium contained 5.0 mM NaH_2PO_4, 20 mM K_2HPO_4, 37 mM NH_4Cl, 17 mM NaCl, 0.81 mM $MgSO_4 \cdot 7H_2O$, and 34 µM $CaCl_2 \cdot 2H_2O$. Addition of essential trace metal nutrients and $FeSO_4$ (30 µM) to the nutrient medium was done prior to inoculation. As previously described [60], after initial inoculation of the culture in glass tubes at 30 °C with shaking at 220 rpm overnight in an incubator-shaker (New Brunswick Scientific, Edison, NJ). The cells were harvested, washed and subsequently transferred into 125-mL or 250-mL baffled flasks. To optimize oxygen transfer, only one-fifth of the volume of the baffled flask was filled with the minimal nutrient medium with carbon source. Cell growth was monitored by measuring the optical density at 600 nm (OD_{600}) using an Agilent Cary UV-Vis spectrophotometer (Santa Clara, CA). Cell dry weight per gram (g_{CDW}) was measured by weighing the mass of lyophilized cell pellets collected throughout the growth as previously described[60]. The conversion factor of OD_{600} and g_{CDW} was calculated through linear regression with R^2 coefficient greater than 0.80 as previously described[60,84]. All growth experiments were conducted in three biological replicates.

Mutant construction. Construction details for strains, oligonucleotides, and plasmids are detailed in Tables S6-S8. In brief, all plasmids were synthesized and cloned by Twist Biosciences. Ribosome binding sites were optimized for each native *P. putida* KT2440 sequence as described previously[85]. For the construction of *P. putida* strains, the parent strain *P. putida* AG5577 containing a total of nine unique attB sites was used as described previously[86]. The parental strain *P. putida* AG5577 was confirmed to be identical to the wild-type *P. putida* KT2440 in phenolic acid utilization (Fig. S2). All integrations were achieved by serine recombinase-assisted genome engineering (SAGE) using either the BxB1 or TG1 recombinase as previously established[86–88]. Integrations were confirmed using Oxford Nanopore sequencing at Plasmidsaurus (https://www.plasmidsaurus.com).

Measuring extracellular substrate depletion. Aliquots of cell suspensions were collected and spanned at different time points throughout biomass growth. Following filtering during centrifugation (Costar Spin-X, 0.22-µm-pore-size filter), the filtrates were stored at -20 °C until analysis. The concentration of each aromatic substrate was determined using ultra-high-performance liquid chromatography (UHPLC) with an Agilent ZORBAX Eclipse Plus C18 column (4.6 × 100 mm with 5 µm particle size) and a UV detector at 210 nm for 4HB and VAN detection, and 275 nm for FER and COU detection. The injection volume was 10 µL and the column was maintained at 25 °C. The mobile phase consisted of 0.1% formic acid (eluent A) and 80:10:10 acetonitrile: methanol: H_2O (eluent B) with a flow rate of 0.9 mL $\cdot$ min^{-1}. The gradient of eluent B was set as 0 min, 6%; 6.5 min, 15%; 8.5 min, 25%; 10.75 min, 37.5%; 15.5 min, 65%; 16.25 min, 6%. Extracellular substrate depletion rate, in mmol $g_{CDW}^{-1} h^{-1}$, was determined by regression analysis. The rate of SUC depletion was obtained by Wilkes et al.[60]

Quantitative Proteomics. *Pseudomonas putida* KT2440 was cultured until mid-exponential phase (OD_{600} = 1.0-1.2) using 100 mM C of FER, COU, VAN, 4HB or SUC as the sole carbon source in the nutrient minimal medium. After centrifugation of 2-mL cultures (10000 *g* for 5 min at 4 °C), the cell pellets were washed twice with phosphate-buffered solution (pH = 7.4) followed by quenching with cold methanol (4 °C) and

19

498 incubated on ice for 30 min. The quenched cell suspensions were centrifuged, and the pellets were
499 resuspended in methanol and stored at -80 °C until analysis.

500   The samples were processed with an on-filter in-cell (OFIC) digestion approach as described
501 previously[89]. Briefly, after transferring the samples to E3 filters (CDS Analytical, Oxford, PA), and
502 centrifuging (400 g for 1 min), the filter was washed once with methanol, and treated with 10 mM Tris(2-
503 carboxyethyl)phosphineand and 40 mM chloroacetamide (in 50mM triethylammonium bicarbonate, TEAB),
504 followed by incubating at 45 °C for 10 min. The sample-containing filters were spun to remove liquid,
505 followed by washing once with 50mM TEAB. Subsequently, the samples were digested with Trypsin/LysC
506 mix at 37 °C for 16-18 h. After digestion, the peptides were eluted, pooled, and dried in SpeedVac. The
507 peptides were desalted with StageTips (CDS Analytical, Oxford, PA), dried, and stored at -80 °C until further
508 analysis.

509   The peptides were first loaded onto a trap column (PepMap100 C18, 300 μm × 2 mm with 5 μm particle
510 size; Thermo Scientific) then separated through an analytical column (PepMap100 C18, 50 cm × 75 μm
511 with 3 μm particle size; Thermo Scientific) with eluents consisting of 0.1% formic acid in water (eluent A)
512 and 0.1% formic acid in acetonitrile (eluent B) with a flow rate of 250 nL · min^{-1} using an Ultimate 3000
513 RSLCnano system with nano electrospray ionization for liquid chromatography mass spectrometry analysis
514 (LC-MS). The MS data were acquired on an Orbitrap Eclipse mass spectrometer with FAIMS Pro Interface
515 (Thermo Scientific) at 120K resolution, followed by MS/MS acquisition in data-independent mode following
516 a protocol described previously[90].

517   The mass spectrometry data were processed using Spectronaut software (version 19.1)[91] and a library-
518 free DIA analysis workflow with directDIA+ and the $P.$ $putida$ KT2440 protein sequence (Uniprot 2024
519 release; 5950 sequences). In short, the settings for Pulsar and library generation included: Trypsin/P as
520 specific enzyme; peptide length from 7 to 52 amino acids; allowing 2 missed cleavages; toggle N-terminal
521 M turned on; Carbamidomethyl on C as fixed modification; Oxidation on M and Acetyl at protein N-terminus
522 as variable modifications; FDRs at PSM, peptide and protein level all set to 0.01; Quantity MS level set to
523 MS2, and cross-run normalization turned on. Bioinformatics analyses were performed using Perseus
524 software (version 1.6.2.3)[92]. The MS raw files obtained for this study have been deposited to the MassIVE
525 server (https://massive.ucsd.edu/) with the accession number MSV000095008. The full dataset of
526 proteomics is provided in Supplemental Dataset 1.

527 **Intracellular metabolite levels and isotope labeling kinetics.** To profile the intracellular metabolites of
528 each of the substrate condition (100 mM C of FER, COU, VAN, 4HB or SUC), cell suspensions (3 mL) of $P.$
529 $putida$ KT2440 during mid-exponential growth phase (OD$_{600}$ = 1.0-1.2) were filtered (0.22 μm nylon
530 membranes; Whatman, 7402-004), then lysed in a cold quenching solution (4 °C) containing methanol,
531 acetonitrile, and water in a 2:2:1 ratio. The suspensions were centrifuged (10000 × g, 4 °C for 5 min) and
532 aliquots (200 μL) of the supernatants in 2mL-tubes were dried under ultrapure nitrogen gas followed by
533 storage at -80 °C before further analysis. The dried samples, collected from four biological replicates, were
534 resuspended in 100 μL LC-MS grade water before metabolomics analysis.

535   In preparation for kinetic ^{13}C-labeling experiments, 3-mL exponentially-growing $P.$ $putida$ KT2440 cells
536 (two transfers, three biological replicates) on each unlabeled substrate (100 mM C of FER, COU, VAN, 4HB,
537 or SUC) were filtered (0.22 μm nylon membranes; Whatman, 7402-004), and the filters containing the cells
538 were placed onto agar plates containing 100 mM C of the same substrate, followed by incubation at 30 °C
539 until exponential growth was resumed. To initiate ^{13}C-labeling of intracellular metabolites, cell-containing
540 filters were transferred onto fresh agar plates with 50% of ^{13}C-labeled substrate: ^{13}C$_6$-phenyl-FER, ^{13}C$_6$-
541 phenyl-COU, ^{13}C$_6$-phenyl-VAN, ^{13}C$_6$-phenyl-4HB, or U^{13}C$_4$-succinate. These labeled substrates were

542 purchased from Cambridge Isotopes (Tewksbury, MA) or Sigma-Aldrich (St. Louis, MO). At four different
543 time points (15 s, 1 min, 5 min, and 15 min), cells adhered to the filter were quenched into the
544 aforementioned cold quenching solution (4 $^{\circ}$C); data for time 0 were obtained with cells directly quenched
545 from the unlabeled plate. The quenched cell suspensions were processed following the aforementioned
546 nitrogen drying procedure and the extracted metabolites were stored at -80 °C until metabolomics analysis.

547 **Metabolomics analysis.** Intracellular and extracellular metabolites were quantified based on our
548 established metabolomics protocol using UHPLC (Thermo Fisher Scientific Dionex UltiMate 3000) coupled
549 with high-resolution mass spectrometry (Thermo Fisher Scientific Q Exactive quadrupole-Orbitrap)
550 operating in negative mode[60,93]. The LC column, an Acquity UPLC BEH C18 Column (particle size 1.7 µm,
551 2.1 mm × 100 mm, Waters), was maintained at 25 °C with an injection volume of 10 µL. The eluents were
552 adopted as previously described with a flow rate of 0.18 mL·min^{-1} [93]. The data was analyzed on the Thermo
553 Scientific XCalibur software (v3.0) using a series of standard concentrations. The fraction of different
554 isotopomers was analyzed using the Metabolomic Analysis and Visualization Engine (MAVEN) software
555 version 2011.6.17[94]; to correct for the natural abundance of ^{13}C, IsoCor v2.2.0[95] was used. The MS data for
556 metabolomics have been deposited to MetaboLights depository (https://www.ebi.ac.uk/metabolights/)
557 under the accession number of MTBLS11484. The full dataset of kinetic ^{13}C-metabolomics is provided in
558 Supplemental Dataset 2.

559 **^{13}C-fluxomics analysis.** We employed both the levels and the kinetic isotopic profiling of intracellular
560 metabolites to perform an isotope non-steady state metabolic flux analysis (INST-MFA) [96]. A core *P. putida*
561 metabolic network was constructed based on published resources with modifications to supplement
562 aromatics utilization pathways[58,61]. The biomass yield equation was modified from a previous genome
563 scale model for *P. putida* KT2440[97]. The INCA software (v2.3) based on Matlab platform[98] was used to
564 simulate isopotomer balances when *P. putida* was fed on different aromatic substrates and succinate. The
565 INST-MFA models were constrained with growth, substrate consumption and metabolite secretion rates,
566 measured pool sizes (CIT, AKG, SUC, PYR, PEP, 3PG, G6P, AcCoA) and kinetic isotopomer distributions
567 (CIT, AKG, SUC, OAA as Asp, PEP, PYR, 3PG, DHAP, G6P, S7P, AcCoA). Flux estimations were reiterated
568 at least 50 times from random initial values as previously suggested to obtain the best fits[99]. At least three
569 independent flux estimations were performed for each INST-MFA model to ensure the flux estimations
570 were consistent. The estimates were considered as statistically acceptable fits when the results passed
571 the χ^2 goodness-of-fit test (cutoff 95% confidence level), i.e., the minimized variance-weighted sum of
572 squared residuals (SSR) were within the expected range. The standard errors (95% confidence intervals)
573 of the flux estimations for the reactions in the central carbon metabolism were calculated through Monte
574 Carlo simulations as previously reported[61,98]. Complete flux estimations are in Supplemental Dataset 3.
575 Cofactor balance was calculated from quantified fluxes for metabolic reactions with production or
576 consumption of NADPH, NADH/UQH$_2$, and ATP. Only NADH was included for vanillate *O*-demethylase
577 because VanB was shown to prefer NADH over NADPH[28].

578 **Flux balance analysis.** The most recent genome-scale model of *P. putida* KT2440 (iJN1463) was
579 downloaded from the BIGG database (http://bigg.ucsd.edu/)[97]. The FER, VAN, and 4HB catabolic reactions
580 are present in the original iJN1463 model. The COU uptake and initial catabolic reactions to coumaroyl-
581 CoA were added manually to the model. The optimized flux distribution predicted by flux balance analysis
582 was performed using the COBRApy library (version 0.29.1)[100]. Substrate uptake rates for SUC, FER, COU,

583 VAN, and 4HB were fixed at the experimentally determined values (in mmol/g$_{CDW}$/h), which are 16.0, 6.7,
584 9.9, 8.2, and 15.9, respectively. For the 4HB analysis, the PCA secretion rate was fixed at 1.2 mmol/g$_{CDW}$/h
585 as experimentally measured. Results for flux balance analysis are in Supplemental Dataset 4.

586 **Statistical analysis.** Unpaired two-tailed *t*-test was applied to evaluate the significance of differences
587 between two groups. One-way analysis of variance (ANOVA) was used to evaluate differences among
588 three or more conditions. Tukey's honestly significant difference (HSD) post hoc test was performed for
589 pairwise comparison in addition to one-way ANOVA. The *P*-value threshold for statistically significant
590 difference was set at 0.05.

591

592 **References**
593 1. Ragauskas, A. J. *et al.* Lignin valorization: improving lignin processing in the biorefinery. *Science* **344**,
594   1246843 (2014).
595 2. Beckham, G. T., Johnson, C. W., Karp, E. M., Salvachúa, D. & Vardon, D. R. Opportunities and
596   challenges in biological lignin valorization. *Curr Opin Biotechnol* **42**, 40–53 (2016).
597 3. Abdelaziz, O. Y. *et al.* Biological valorization of low molecular weight lignin. *Biotechnol Adv* **34**, 1318–
598   1346 (2016).
599 4. Kamimura, N. *et al.* Bacterial catabolism of lignin-derived aromatics: New findings in a recent decade:
600   Update on bacterial lignin catabolism. *Environ Microbiol Rep* **9**, 679–705 (2017).
601 5. Sun, Z., Fridrich, B., de Santi, A., Elangovan, S. & Barta, K. Bright side of lignin depolymerization:
602   toward new platform chemicals. *Chem. Rev.* **118**, 614–678 (2018).
603 6. Xu, R. *et al.* Lignin depolymerization and utilization by bacteria. *Bioresour Technol* **269**, 557–566
604   (2018).
605 7. Becker, J. & Wittmann, C. A field of dreams: Lignin valorization into chemicals, materials, fuels, and
606   health-care products. *Biotechnol Adv* **37**, 107360 (2019).
607 8. Anthony, W. E. *et al.* Development of Rhodococcus opacus as a chassis for lignin valorization and
608   bioproduction of high-value compounds. *Biotechnol Biofuels* **12**, 192 (2019).
609 9. Schutyser, W. *et al.* Chemicals from lignin: an interplay of lignocellulose fractionation,
610   depolymerisation, and upgrading. *Chem. Soc. Rev.* **47**, 852–908 (2018).
611 10. Tack, B. F., Chapman, P. J. & Dagley, S. Metabolism of gallic acid and syringic acid by *Pseudomonas
612   putida*. *J Biol Chem* **247**, 6438–6443 (1972).
613 11. Turner, J. e. & Allison, N. Degradation of methoxylated aromatic acids by *Pseudomonas putida*. *J Appl
614   Bacteriol* **78**, 125–133 (1995).
615 12. Reber, H. H. Regulation of the utilization of 4-hydroxybenzoate and vanillate in batch and continuous
616   cultures of *Pseudomonas acidovorans*. *Arch. Microbiol.* **126**, 65–70 (1980).
617 13. Jiménez, J. I., Miñambres, B., García, J. L. & Díaz, E. Genomic analysis of the aromatic catabolic
618   pathways from *Pseudomonas putida* KT2440. *Environ Microbiol* **4**, 824–841 (2002).
619 14. Cao, B. & Loh, K.-C. Catabolic pathways and cellular responses of *Pseudomonas putida* P8 during
620   growth on benzoate with a proteomics approach. *Biotechnol Bioeng* **101**, 1297–1312 (2008).
621 15. Xie, N. *et al.* Characterization of benzoate degradation by newly isolated bacterium *Pseudomonas* sp.
622   XP-M2. *Biochem Eng J* **46**, 79–82 (2009).
623 16. Chen, S.-Y. *et al.* Biodegradation of p-hydroxybenzoic acid in soil by *Pseudomonas putida* CSY-P1
624   isolated from cucumber rhizosphere soil. *Plant Soil* **389**, 197–210 (2015).
625 17. Sudarsan, S. *et al.* Dynamics of benzoate metabolism in *Pseudomonas putida* KT2440. *Metab Eng
626   Commun* **3**, 97–110 (2016).
627 18. Kukurugya, M. A. *et al.* Multi-omics analysis unravels a segregated metabolic flux network that tunes
628   co-utilization of sugar and aromatic carbons in *Pseudomonas putida*. *J Biol Chem* **294**, 8464–8479
629   (2019).
630 19. Nikel, P. I. & de Lorenzo, V. *Pseudomonas putida* as a functional *chassis* for industrial biocatalysis:
631   From native biochemistry to *trans*-metabolism. *Metab Eng* **50**, 142–155 (2018).

20. Schwanemann, T., Otto, M., Wierckx, N. & Wynands, B. *Pseudomonas* as Versatile Aromatics Cell Factory. *Biotechnol J* **15**, 1900569 (2020).

21. de Lorenzo, V., Pérez-Pantoja, D. & Nikel, P. I. *Pseudomonas putida* KT2440: the long journey of a soil-dweller to become a synthetic biology chassis. *J Bacteriol* **0**, e00136-24 (2024).

22. Silva, M., Donati, S. & Dvořák, P. Advances in engineering substrate scope of *Pseudomonas* cell factories. *Current Opinion in Biotechnology* **92**, 103270 (2025).

23. Narbad, A. & Gasson, M. J. Metabolism of ferulic acid via vanillin using a novel CoA-dependent pathway in a newly-isolated strain of *Pseudomonas fluorescens*. *Microbiology* **144**, 1397–1405 (1998).

24. Salvachúa, D. *et al.* Outer membrane vesicles catabolize lignin-derived aromatic compounds in *Pseudomonas putida* KT2440. *Proc Natl Acad Sci USA* **117**, 9302–9310 (2020).

25. Erickson, E. *et al.* Critical enzyme reactions in aromatic catabolism for microbial lignin conversion. *Nat Catal* **5**, 86–98 (2022).

26. Nichols, N. N. & Harwood, C. S. PcaK, a high-affinity permease for the aromatic compounds 4-hydroxybenzoate and protocatechuate from *Pseudomonas putida*. *J Bacteriol* **179**, 5056–5061 (1997).

27. Wada, A. *et al.* Characterization of aromatic acid/proton symporters in *Pseudomonas putida* KT2440 toward efficient microbial conversion of lignin-related aromatics. *Metab Eng* **64**, 167–179 (2021).

28. Bleem, A. C. *et al.* Evolution and engineering of pathways for aromatic *O*-demethylation in *Pseudomonas putida* KT2440. *Metab Eng* **84**, 145–157 (2024).

29. Linger, J. G. *et al.* Lignin valorization through integrated biological funneling and chemical catalysis. *Proc Natl Acad Sci USA* **111**, 12013–12018 (2014).

30. Graf, N. & Altenbuchner, J. Genetic engineering of *Pseudomonas putida* KT2440 for rapid and high-yield production of vanillin from ferulic acid. *Appl Microbiol Biotechnol* **98**, 137–149 (2014).

31. Vardon, D. R. *et al.* Adipic acid production from lignin. *Energy Environ. Sci.* **8**, 617–628 (2015).

32. Okamura-Abe, Y. *et al.* Beta-ketoadipic acid and muconolactone production from a lignin-related aromatic compound through the protocatechuate 3,4-metabolic pathway. *J Biosci Bioeng* **121**, 652–658 (2016).

33. Salvachúa, D. *et al.* Bioprocess development for muconic acid production from aromatic compounds and lignin. *Green Chem.* **20**, 5007–5019 (2018).

34. Kohlstedt, M. *et al.* From lignin to nylon: Cascaded chemical and biochemical conversion using metabolically engineered *Pseudomonas putida*. *Metab Eng* **47**, 279–293 (2018).

35. Johnson, C. W. *et al.* Innovative Chemicals and Materials from Bacterial Aromatic Catabolic Pathways. *Joule* **3**, 1523–1537 (2019).

36. Salvachúa, D. *et al.* Metabolic engineering of *Pseudomonas putida* for increased polyhydroxyalkanoate production from lignin. *Microb Biotechnol* **13**, 290–298 (2020).

37. Almqvist, H. *et al.* Muconic acid production using engineered *Pseudomonas putida* KT2440 and a guaiacol-rich fraction derived from kraft lignin. *ACS Sustainable Chem. Eng.* **9**, 8097–8106 (2021).

38. Upadhyay, P. & Lali, A. Protocatechuic acid production from lignin-associated phenolics. *Prep Biochem Biotechnol* **51**, 979–984 (2021).

39. Eng, T. *et al.* Engineering *Pseudomonas putida* for efficient aromatic conversion to bioproduct using high throughput screening in a bioreactor. *Metabolic Engineering* **66**, 229–238 (2021).

40. Werner, A. Z. *et al.* Lignin conversion to β-ketoadipic acid by *Pseudomonas putida* via metabolic engineering and bioprocess development. *Sci Adv* **9**, eadj0053 (2023).

41. Liu, H. *et al.* Engineering *Pseudomonas putida* for lignin bioconversion into *cis-cis* muconic acid. *Chem Eng J* **495**, 153375 (2024).

42. Banerjee, D. *et al.* Addressing genome scale design tradeoffs in Pseudomonas putida for bioconversion of an aromatic carbon source. *npj Syst Biol Appl* **11**, 1–13 (2025).

43. Kuatsjah, E. *et al.* Debottlenecking 4-hydroxybenzoate hydroxylation in *Pseudomonas putida* KT2440 improves muconate productivity from p-coumarate. *Metab Eng* **70**, 31–42 (2022).

682   44. Gómez-Álvarez, H. *et al.* Bioconversion of lignin-derived aromatics into the building block pyridine
683   2,4-dicarboxylic acid by engineering recombinant *Pseudomonas putida* strains. *Bioresour Technol*
684   **346**, 126638 (2022).
685   45. Johnson, C. W. *et al.* Eliminating a global regulator of carbon catabolite repression enhances the
686   conversion of aromatic lignin monomers to muconate in *Pseudomonas putida* KT2440. *Metab Eng*
687   *Commun* **5**, 19–25 (2017).
688   46. Wiechert, W., Möllney, M., Petersen, S. & de Graaf, A. A. A Universal Framework for 13C Metabolic
689   Flux Analysis. *Metab Eng* **3**, 265–283 (2001).
690   47. Wiechert, W. 13C Metabolic Flux Analysis. *Metabolic Engineering* **3**, 195–206 (2001).
691   48. Nöh, K. *et al.* Metabolic flux analysis at ultra short time scale: Isotopically non-stationary 13C labeling
692   experiments. *Journal of Biotechnology* **129**, 249–267 (2007).
693   49. Wiechert, W. & Nöh, K. Isotopically non-stationary metabolic flux analysis: complex yet highly
694   informative. *Current Opinion in Biotechnology* **24**, 979–986 (2013).
695   50. Hollinshead, W. D., Henson, W. R., Abernathy, M., Moon, T. S. & Tang, Y. J. Rapid metabolic analysis of
696   Rhodococcus opacus PD630 via parallel 13C-metabolite fingerprinting. *Biotechnology and*
697   *Bioengineering* **113**, 91–100 (2016).
698   51. Hendry, J. I. *et al.* Metabolic flux analysis reaching genome wide coverage: lessons learned and future
699   perspectives. *Curr Opin Chem Eng* **30**, 17–25 (2020).
700   52. Sacco, S. A. & Young, J. D. 13C metabolic flux analysis in cell line and bioprocess development. *Curr*
701   *Opin Chem Eng* **34**, 100718 (2021).
702   53. Antoniewicz, M. R. A guide to metabolic flux analysis in metabolic engineering: Methods, tools and
703   applications. *Metab Eng* **63**, 2–12 (2021).
704   54. Ebert, B. E., Kurth, F., Grund, M., Blank, L. M. & Schmid, A. Response of *Pseudomonas putida* KT2440
705   to Increased NADH and ATP Demand. *Appl Environ Microbiol* **77**, 6597–6605 (2011).
706   55. Chavarría, M., Kleijn, R. J., Sauer, U., Pflüger-Grau, K. & de Lorenzo, V. Regulatory Tasks of the
707   Phosphoenolpyruvate-Phosphotransferase System of *Pseudomonas putida* in Central Carbon
708   Metabolism. *mBio* **3**, 10.1128/mbio.00028-12 (2012).
709   56. Nikel, P. I., Chavarría, M., Fuhrer, T., Sauer, U. & de Lorenzo, V. *Pseudomonas putida* KT2440 strain
710   metabolizes glucose through a cycle formed by enzymes of the Entner-Doudoroff, Embden-Meyerhof-
711   Parnas, and Pentose Phosphate pathways. *J Biol Chem* **290**, 25920–25932 (2015).
712   57. Sasnow, S. S., Wei, H. & Aristilde, L. Bypasses in intracellular glucose metabolism in iron-limited
713   *Pseudomonas putida*. *MicrobiologyOpen* **5**, 3–20 (2016).
714   58. Kohlstedt, M. & Wittmann, C. GC-MS-based 13C metabolic flux analysis resolves the parallel and
715   cyclic glucose metabolism of *Pseudomonas putida* KT2440 and Pseudomonas aeruginosa PAO1.
716   *Metab Eng* **54**, 35–53 (2019).
717   59. Nikel, P. I. *et al.* Reconfiguration of metabolic fluxes in *Pseudomonas putida* as a response to sub-
718   lethal oxidative stress. *ISME J* **15**, 1751–1766 (2021).
719   60. Wilkes, R. A., Waldbauer, J. & Aristilde, L. Analogous metabolic decoupling in *Pseudomonas putida*
720   and *Comamonas testosteroni* implies energetic bypass to facilitate gluconeogenic growth. *mBio* **12**,
721   e03259-21 (2021).
722   61. Czajka, J. J. *et al.* Tuning a high performing multiplexed-CRISPRi *Pseudomonas putida* strain to
723   further enhance indigoidine production. *Metab Eng Commun* **15**, e00206 (2022).
724   62. Vogeleer, P. *et al.* Metabolic impact of heterologous protein production in *Pseudomonas putida*:
725   Insights into carbon and energy flux control. *Metab Eng* **81**, 26–37 (2024).
726   63. Dvořák, P. *et al.* Synthetically-primed adaptation of *Pseudomonas putida* to a non-native substrate D-
727   xylose. *Nat Commun* **15**, 2666 (2024).
728   64. Wang, J. H. The molecular mechanism of oxidative phosphorylation. *Proc Natl Acad Sci USA* **58**, 37–
729   44 (1967).
730   65. Bonora, M. *et al.* ATP synthesis and storage. *Purinergic Signal* **8**, 343–357 (2012).
731   66. Owen, O. E., Kalhan, S. C. & Hanson, R. W. The key role of anaplerosis and cataplerosis for citric acid
732   cycle function. *J Biol Chem* **277**, 30409–30412 (2002).

67. Belda, E. *et al.* The revisited genome of *Pseudomonas putida* KT2440 enlightens its value as a robust metabolic chassis. *Environ Microbiol* **18**, 3403–3424 (2016).

68. Koendjbiharie, J. G., van Kranenburg, R. & Kengen, S. W. M. The PEP-pyruvate-oxaloacetate node: variation at the heart of metabolism. *FEMS Microbiol Rev* **45**, fuaa061 (2021).

69. Ramos-González, M.-I., Godoy, P., Alaminos, M., Ben-Bassat, A. & Ramos, J.-L. Physiological Characterization of Pseudomonas putida DOT-T1E Tolerance to p-Hydroxybenzoate. *Appl Environ Microbiol* **67**, 4338–4341 (2001).

70. Hibi, M., Sonoki, T. & Mori, H. Functional coupling between vanillate-O-demethylase and formaldehyde detoxification pathway. *FEMS Microbiol Lett* **253**, 237–242 (2005).

71. Roca, A., Rodríguez-Herva, J. J. & Ramos, J. L. Redundancy of enzymes for formaldehyde detoxification in *Pseudomonas putida*. *J Bacteriol* **191**, 3367–3374 (2009).

72. Ramos, J. L. *et al.* Mechanisms of Solvent Tolerance in Gram-Negative Bacteria. *Annual Review of Microbiology* **56**, 743–768 (2002).

73. Dunlop, M. J. *et al.* Engineering microbial biofuel tolerance and export using efflux pumps. *Molecular Systems Biology* **7**, 487 (2011).

74. Mendonca, C. M. *et al.* Hierarchical routing in carbon metabolism favors iron-scavenging strategy in iron-deficient soil *Pseudomonas* species. *Proc Natl Acad Sci USA* **117**, 32358–32369 (2020).

75. Wilkes, R. A. *et al.* Complex regulation in a *Comamonas* platform for diverse aromatic carbon metabolism. *Nat Chem Biol* 1–12 (2023) doi:10.1038/s41589-022-01237-7.

76. Mohamed, E. T. *et al.* Adaptive laboratory evolution of *Pseudomonas putida* KT2440 improves *p*-coumaric and ferulic acid catabolism and tolerance. *Metab Eng Commun* **11**, e00143 (2020).

77. Kasai, D. *et al.* Uncovering the Protocatechuate 2,3-Cleavage Pathway Genes. *J Bacteriol* **191**, 6758–6768 (2009).

78. Harayama, S. & Rekik, M. The meta cleavage operon of TOL degradative plasmid pWWO comprises 13 genes. *Mol Gen Genet* **221**, 113–120 (1990).

79. Kamimura, N. & Masai, E. The Protocatechuate 4,5-Cleavage Pathway: Overview and New Findings. in *Biodegradative Bacteria: How Bacteria Degrade, Survive, Adapt, and Evolve* (eds. Nojiri, H., Tsuda, M., Fukuda, M. & Kamagata, Y.) 207–226 (Springer Japan, Tokyo, 2014). doi:10.1007/978-4-431-54520-0_10.

80. Varman, A. M. *et al.* Decoding how a soil bacterium extracts building blocks and metabolic energy from ligninolysis provides road map for lignin valorization. *Proc Natl Acad Sci USA* **113**, E5802–E5811 (2016).

81. Borrero-de Acuña, J. M. *et al.* Channelling carbon flux through the meta-cleavage route for improved poly(3-hydroxyalkanoate) production from benzoate and lignin-based aromatics in Pseudomonas putida H. *Microb Biotechnol* **14**, 2385–2402 (2021).

82. Salvachúa, D., M. Karp, E., T. Nimlos, C., R. Vardon, D. & T. Beckham, G. Towards lignin consolidated bioprocessing: simultaneous lignin depolymerization and product generation by bacteria. *Green Chem* **17**, 4951–4967 (2015).

83. Karp, E. *et al.* Quantification of acidic compounds in complex biomass-derived streams. *Green Chem* **18**, 4750–4760 (2016).

84. Sasnow, S. S., Wei, H. & Aristilde, L. Bypasses in intracellular glucose metabolism in iron-limited Pseudomonas putida. *MicrobiologyOpen* **5**, 3–20 (2016).

85. Cetnar, D. P. & Salis, H. M. Systematic Quantification of Sequence and Structural Determinants Controlling mRNA stability in Bacterial Operons. *ACS Synth. Biol.* **10**, 318–332 (2021).

86. Schmidt, M. *et al.* Maximizing heterologous expression of engineered Type I polyketide synthases: investigating codon optimization strategies. *ACS Synth Biol* **12**, 3366–3380 (2023).

87. Werner, A. Z. *et al.* Tandem chemical deconstruction and biological upcycling of poly(ethylene terephthalate) to β-ketoadipic acid by Pseudomonas putida KT2440. *Metab Eng* **67**, 250–261 (2021).

88. Elmore, J. R. *et al.* High-throughput genetic engineering of nonmodel and undomesticated bacteria via iterative site-specific genome integration. *Science Advances* **9**, eade1285 (2023).

89. Martin, K. R. *et al.* Development of an efficient, effective, and economical technology for proteome analysis. *Cell Rep Methods* **4**, 100796 (2024).

90. Reilly, L. *et al.* A fully automated FAIMS-DIA mass spectrometry-based proteomic pipeline. *Cell Reports Methods* **3**, 100593 (2023).

91. Bruderer, R. *et al.* Extending the Limits of Quantitative Proteome Profiling with Data-Independent Acquisition and Application to Acetaminophen-Treated Three-Dimensional Liver Microtissues. *Mol Cell Proteomics* **14**, 1400–1410 (2015).

92. Tyanova, S. *et al.* The Perseus computational platform for comprehensive analysis of (prote)omics data. *Nature Methods* **13**, 731–740 (2016).

93. Aristilde, L. *et al.* Glyphosate-Induced Specific and Widespread Perturbations in the Metabolome of Soil Pseudomonas Species. *Frontiers in Environmental Science* **5**, (2017).

94. Clasquin, M. F., Melamud, E. & Rabinowitz, J. D. LC-MS Data Processing with MAVEN: A Metabolomic Analysis and Visualization Engine. *Curr Protoc Bioinformatics* **0 14**, Unit14.11 (2012).

95. Millard, P. *et al.* IsoCor: isotope correction for high-resolution MS labeling experiments. *Bioinformatics* **35**, 4484–4487 (2019).

96. Jazmin, L. J. & Young, J. D. Isotopically nonstationary 13C metabolic flux analysis. *Methods Mol Biol* **985**, 367–390 (2013).

97. Nogales, J. *et al.* High-quality genome-scale metabolic modelling of *Pseudomonas putida* highlights its broad metabolic capabilities. *Environ Microbiol* **22**, 255–269 (2020).

98. Young, J. D. INCA: a computational platform for isotopically non-stationary metabolic flux analysis. *Bioinformatics* **30**, 1333–1335 (2014).

99. Ma, F., Jazmin, L. J., Young, J. D. & Allen, D. K. Isotopically nonstationary 13C flux analysis of changes in Arabidopsis thaliana leaf metabolism due to high light acclimation. *Proceedings of the National Academy of Sciences* **111**, 16967–16972 (2014).

100. Ebrahim, A., Lerman, J. A., Palsson, B. O. & Hyduke, D. R. COBRApy: COnstraints-Based Reconstruction and Analysis for Python. *BMC Syst Biol* **7**, 74 (2013).

Acknowledgments

Author contributions

N.Z., R.A.W., X.C., K.P.T., J.A.B., and Y.Y. performed research. G.T.B and A.Z.W provided resources. N.Z. and L.A. designed research, analyzed data, and wrote manuscript. L.A. supervised research.

Competing interests:

830   The authors declare no competing interests.

831

Data and materials availability

833   Proteomics data and metabolomics MS data are freely available in the MassIVE server

834   (https://massive.ucsd.edu/) and MetaboLights depository (https://www.ebi.ac.uk/metabolights/) under

835   accession numbers MSV000095008 and MTBLS11484, respectively.

836

Supplemental Materials

838   The SI document contains:

839   Figures S1-S5

840   Tables S1-S8

841   Supplemental Dataset 1

842   Supplemental Dataset 2

843   Supplemental Dataset 3

844   Supplemental Dataset 4